Optimizing multiplexed imaging experimental design through tissue spatial segregation estimation

Pierre Bost[1,2], Daniel Schulz[1,2], Stefanie Engler[1,2], Clive Wasserfall[3], and Bernd Bodenmiller[1,2]*

[1] University of Zurich, Department of Quantitative Biomedicine, Zurich, 8057, Switzerland

[2] ETH Zurich, Institute for Molecular Health Sciences, Zurich, 8093 Switzerland

[3] Department of Pathology, Immunology, and Laboratory Medicine, Diabetes Institute, University of Florida, Gainesville, FL 32610, USA

* Correspondence: bernd.bodenmiller@uzh.ch

Abstract

Recent advances in multiplexed imaging methods allow simultaneous detection of dozens of proteins or RNAs enabling deep spatial characterization of both healthy and tumor tissues. Parameters for design of optimal sequencing-based experiments have been established, but such parameters are lacking for multiplex imaging studies. Here, using a spatial transcriptomic atlas of healthy and tumor human tissues, we developed a new statistical framework that determines the number of fields of view necessary to accurately identify all cell types that are part of the tissue. Using this strategy on imaging mass cytometry data, we identified a measurement of tissue spatial segregation that enables optimal experimental design and that is technology invariant. This strategy will enable significantly improved design of multiplexed imaging studies.

Main text

In the last decade, single-cell technologies for proteomic (Bendall et al. 2011) and genomic (Jaitin et al. 2014, Macosko et al. 2015**)** analyses have been developed. Experiments using these technologies have furthered expanded our understanding of various biological systems ranging from human immune cells (Villani et al. 2017) to whole cnidarian organisms (Sebé-Pedrós et al. 2018). Clear guidelines have been established for optimal experimental design of sequencing studies, including the total number of sequenced cells and the necessary sequencing depth necessary for detection of rare cell types or transcripts (Torre et al. 2018). Guidelines for optimal design of multiplexed imaging experiments, such as those performed using imaging mass cytometry (IMC) (Giesen et al. 2014) and in situ hybridization methods such as seqFISH (Shah et al. 2016) have not been developed.

Historically, tissue histological analysis has focused on determining whether certain cell types, for instance cells expressing a given oncogene or receptor, are present or absent (Titford 2006). Multiplexed imaging techniques are modern counterparts of histological analyses and, as such, aim to detect a given set of cell types based on the target markers used. Therefore, the ability of a multiplexed imaging experiment to detect every expected cell type that are present in a given tissue section is essential. As it is possible to model the probability of detecting an object when imaging a given area (Illian et al. 2008), there is a solid theoretical foundation for modeling and interpreting the outputs of multiplexed imaging experiments. Here, we report development of a strategy to determine the minimal number of fields of view (FoVs) necessary to identify all main cell types across various healthy and tumor tissues

Using spatial transcriptomic data to determine an optimal tissue sampling strategy

Despite the lack of singe-cell resolution, spatial transcriptomic datasets cover large areas of tissues (16 mm^2 for Visium® arrays) and are assumed to provide an exhaustive description of cell types present in the tissue. We collected 22 Visium datasets on 12 different types of tissues, normalized the data, and performed clustering to identify different cell types and cellular niches (Table S1, Figure 1A). We then simulated a conventional image acquisition by IMC on these same tissues by performing repeated random sampling without replacement of a variable number of non-overlapping small square regions with widths of 400 µm across the tissue. We then computed the number of different clusters (which correspond to unique cell types) detected across the sampled regions. Finally the results were aggregated across samplings. There was an apparent saturation in the detection of clusters as the number of FoVs increased (Figure 1B).

To model the relationship between number of clusters and number of FoVs, we used a model derived from the analysis of homogeneous Poisson point process, the core example of point process theory (Illian et al. 2008) (Figure 1B):

$$N(r) = N_o * (1-\exp(-r/\tau)) \quad (1)$$

where r is the number of FoVs and N(r) the number of recovered clusters. N_o corresponds to the total number of observed clusters and τ indicates how many regions must be imaged to recover most of the known clusters. According to this model, 2τ FoVs must be imaged to detect 86% of known clusters. This model fits particularly well across all samples (Figure S1A), and τ varied significantly across tissues (Figure 1C). Interestingly, we observed that tumor samples have higher τ values than do healthy samples, indicating that more FoVs are required on average to identify known cell types in tumor tissue than in healthy tissue (Figure 1D, p=0.0231).

We next studied the effects of the width of the FoV, w, on spatial sampling efficiency by performing the same simulated IMC analysis with various values of w. As expected, fewer regions needed to be imaged to detect all known clusters when w values were larger (Figure 1E, left panel). There was a linear relationship following logarithmic transformation between w and τ across all studied tissues (Figure 1E, right panel, Figure 1F, and Figure S1B), indicating an underlying power law. Therefore, τ can be written as a function of w:

$$\tau(w) = \mathbf{C}/w^{\alpha} \quad (2)$$

where **C** and $\boldsymbol{\alpha}$ are specific to each sample.

Lastly, we speculated that there would be a relationship between τ and the granularity of the initial clustering analysis. To test this, we aggregated the most similar pairs of clusters for each sample by determining the correlation between mean expression profiles, performed a sampling analysis to compute τ, and then merged the next two most similar clusters, repeating until only two clusters were left (Figure S1C). We observed a linear relationship between τ and the number of clusters in individual samples such as a glioblastoma (Figure 1G), but the linear regression fit poorly for some samples such as for cerebellum (Figure S1D), suggesting that this relationship cannot be generalized. In addition, across all samples, τ and of the number of detected clusters are poorly correlated (Figure 1H, R^2=0.45), suggesting that the number of clusters is not a major determinant of τ.

Identification of a technology invariant measure of tissue spatial segregation

In order to confirm that our results obtained from the analysis of spatial transcriptomic data can be generalized to data obtained from other technologies that provide images at single-cell resolution, we imaged a large section of two human formalin-fixed paraffin-embedded lymph node sections using IMC with two antibody panels (Table S2) and performed a spatial sampling analysis with various FoV widths (Figure 2A). As for the Visium lymph node data, the relationship between the number of sampled regions and of recovered clusters could be modeled using equation (1) (Figure 2B, left panel) and the FoV width affected τ as described by equation (2) (Figure 2B, middle and right panels). However, the values of τ drastically differed between the Visium lymph node data and the two IMC datasets (Figure 2C, left panel). The $\boldsymbol{\alpha}$ parameter did not significantly differ between the two imaging modalities (Figure 2C, middle panel), whereas there was a large difference in **C** (Figure 2C, right panel). There was a large variability with $\boldsymbol{\alpha}$ across tissue types analyzed by spatial transcriptomics with values ranging from 2 for cardiac tissue to 0.91 for breast tumor tissue (Figure S2A). Strikingly, $\boldsymbol{\alpha}$ was significantly lower in cancer samples than healthy tissues (Figure S2A, p=0.0401). These analyses indicate that $\boldsymbol{\alpha}$ is tissue specific and technology independent, whereas **C** is dependent on the technology used to generate the data.

To further validate that $\boldsymbol{\alpha}$ is a technology invariant parameter, we re-analyzed a previously published IMC dataset (Jackson et al. 2020) containing 100 FoVs, each derived from a unique

breast cancer sample. For each FoV, we simulated a progressive shrinkage of the FoV width and computed the effect on the number of detected clusters to obtain an estimate of $\boldsymbol{\alpha}$ for each FoV (Figure S2B). We did not observed a significant difference between the estimated $\boldsymbol{\alpha}$ values using IMC data and the one estimated from five different Visium breast cancer samples (Figure 2D, p=0.699), further supporting our hypothesis that $\boldsymbol{\alpha}$ is a technology-independent parameter.

Lastly, to evaluate the impact of $\boldsymbol{\alpha}$ on the sampling strategy design, we computed the theoretical number of recovered clusters when sampling a defined area with various numbers of FoVs. We performed this analysis on two different types of tissue: cardiac (low spatial heterogeneity, $\boldsymbol{\alpha}$=2) and breast cancer tissue (strong spatial heterogeneity, $\boldsymbol{\alpha}$=0.91). Interestingly, the number of recovered clusters was not affected by the fragmentation of the FoVs for the heart sample. In contrast, for breast cancer samples, a lower number of larger FoVs recovered a significantly lower number of clusters than did measurement of the same area with more, but smaller FoVs (Figure 2E and 2F).

Discussion

Here we report how experimental design parameters impact the efficiency of multiplexed imaging experiments using the proportion of detected cell types as a simple yet robust metric. Our analysis identified the number of FoV and their width as key parameters that drive imaging experiment efficiency as well as the precise mathematical relationship linking these two parameters to the number of detected clusters. Moreover, we found that the impact of FoV width on the experiment efficiency was regulated by a constant term $\boldsymbol{\alpha}$ that is tissue specific and independent of the imaging technology used.

The value of $\boldsymbol{\alpha}$ dramatically varied across tissues and must therefore be taken into account when planning an multiplexed imaging experiment. A value of $\boldsymbol{\alpha}$ close to 2 means that one can image a small number of large FoVs or many small FoVs and detect the same number of cell types. In contrast, a small $\boldsymbol{\alpha}$ value requires the sampling of many small regions. In order to facilitate the planning of imaging experiments, we provide $\boldsymbol{\alpha}$ values for various healthy and cancerous tissues (Table S3).

In practice, one has to balance two constraints: the low efficiency of imaging large FoVs to recover cell types and loss of information on long-range cellular interactions or large structures

such as tertiary lymphoid structures in tumors when small FoVs are evaluated. The ideal FoV width to efficiently recover most cell types and cellular structures thus must be determined for each tissue type.

Beyond application to design of multiplexed imaging experiments, our results could also be used in the field of anapathology in which the current standard for classification of samples is the analysis of one to four circular punches of variable diameter (600µm to 2mm) (Eckel-Passow et al. 2010). Although we focused on the recovery of multiple cell types (i.e., clusters) rather than a single type of cell (for instance, $HER2^+$ cells in breast cancer samples) (Harbeck et al. 2019), it is likely that a similar phenomenon of spatial segregation impairs efficacy of this type of sampling. In summary, our approach provides essential guidance for study of tissue structures using multiplex imaging in a time and cost-efficient manner.

Methods

Visium data pre-processing and analysis

Visium data were downloaded from the 10X Genomics website (support.10xgenomics.com/spatial-gene-expression/datasets/), the Gene Expression Omnibus (GEO), or the Zenodo data portals. Spots with less than 1000 UMIs as well as genes with less than 100 UMIs were removed before any analysis. Data were analyzed by combining the classical scRNA-seq pipeline **Pagoda2** (Lake et al. 2018) with a latent Dirichlet allocation analysis step. Briefly, the top 1500 most variable genes were identified using the adjustvariance() function from **Pagoda2** package, and the raw count data matrix containing only these genes was processed using the FitGoM() function from the **CountClust** package with a tolerance parameter set to 100 and the number of topics set to 5, 10, 15, or 20. For each number of topics, the BIC score was computed, and the number of topics displaying the lowest BIC or an elbow-like inflection was selected. The mixing matrix was then used for the next steps of analysis. A *k*-nearest-neighbor graph was built using the makeKnnGraph() function with parameter *k* set to 15 and using a cosine distance before performing a community detection analysis with the getKnnClusters() function with default parameters (corresponding to Louvain's community detection (Blondel et al. 2008)).

Spatial sampling analysis

To simulate spatial sampling strategies, we created a simple function that iteratively selects a random point on the sample, 'draws' a square with the sampled point at the center, and then checks whether this square overlaps with previously sampled squares. In case of overlap, the point is removed and a new point is sampled. A cluster was considered as detected by a given spatial sampling (set of sampled FoVs) if more than T spots belonging to that cluster were located in the drawn squares. The threshold T was changed based on the type of data: It was set to 2 for Visium data, 50 for the IMC lymph node data, and 20 for the IMC breast cancer data. This sampling was repeated 50 times in order to get a robust estimate .

The model proposed in equation (1) was derived from the analysis of a homogenous Poisson point (HPP) process defined by a density parameter λ. The probability that a random square of size w contain no points is equal to $\exp(-\lambda w^2)$. A basic property of HPP processes is that the probability of finding no points in r independent (i.e., non-overlapping) squares is $\exp(-\lambda r w^2)$, and therefore the probability of finding at least one point is $1-\exp(-\lambda n w^2)$. As we are looking at N_o different clusters (i.e., N_o different point processes), the mean number of detected clusters for a fixed number of squares N(r) is $N_o = 1-\exp(-\lambda r w^2)$, thus justifying the use of equation (1).

In order to fit the model described in equation (1), we used the nls() function with the following starting values: N_o of 20 and τ of 5. The quality of the fit was estimated using cor() and predict() functions. Fitting equation (2) to the data was done by first applying a log10 transform to the data before performing a classical least square regression using the lm() R function.

In order to study the effects of clustering granularity on cluster recovery, we first computed the mean expression of each gene in each cluster, then built a hierarchical clustering tree using Euclidean distance and Ward's criterion. Then, using this tree, we iteratively merged the different clusters and at each step performed a spatial sampling analysis.

Lymph node section processing and IMC data acquisition

The two lymph node formalin-fixed, paraffin-embedded blocks were first cut into 5-µm thick sections. They were then dewaxed and rehydrated and subjected to a heat-induced epitope retrieval step for 30 minutes at 95 ºC in 10 mM Tris, pH 9.2, 1 mM EDTA. The sections were then incubated in blocking buffer (3% BSA in TBS-T) for 1 hour at room temperature, before incubation with the antibody panel (diluted in blocking buffer) overnight at 4 ºC. Nuclear staining was then performed by adding an iridium solution (5 nM) diluted in TBS (1:100 dilution) to the sample and incubating for 5 minutes. The samples were then washed three times (10 minutes per wash) in TBS

and dried. Images were acquired using an Hyperion Imaging System with the ablation frequency set to 200 Hz and the ablation energy to 6 dB with a X and Y step set to 1 µm.

IMC data pre-processing and analysis

The raw Mcd files were processed using the Steinbock pipeline (Windhager et al. 2021). In brief, the raw files were converted into tiff files, and the cells were segmented using a pre-trained neural network (Greenwald et al. 2021) using the H3K9ac channel as the nuclear channel and CD45RA/RO and Vimentin genes as the membrane channels. Default parameters were used for Mesmer, except the —type parameter, which was set to 'nuclei'. The mean channel intensity was then computed for each cell and exported as a text file, together with the location, the size, and other basic information on the cells. The single-cell IMC data were then analyzed using in-house R scripts (R version 4.0.3). Each channel was normalized by performing a Poisson regression between the total channel intensity and the cell size (in pixels); the Pearson's residuals were extracted as the new scaled values. The cells were then clustered by first building a *k*-nearest-neighbor graph with 15 neighbors (using cosine distance) and then clustered using Louvain's community detection implemented in the **igraph** package.

Breast cancer IMC data re-analysis

The SingleCellExperiment object containing single-cell information from 100 FoVs, each one derived from a different sample was downloaded from the Zenodo platform and analyzed using the following strategy: We first aggregated all cancer clusters (clusters 14 to 27) into a single cluster as the cancer clusters displayed a strong patient specificity. For each FoV, we progressively reduced the size of the image by factors of 1.1, 1.2, 1.5, 1.8, 2.2, 2.5, and 3 and computed the number of detected clusters. We then performed a linear regression between the log transformed number of detected clusters and the size of the reduced FoV using the lm() core function. FoVs with a low-quality model (R^2 <0.9) were removed, and the slope of the regression was taken as the estimate of α. If we combine equations (1) and (2) when considering a single FoV, we have:

$$N(1) = N_o * (1-\exp(-1/\tau)) \quad (3)$$

$$\text{Therefore : } \log(1-N(1)/N_o) = (-1/\tau) = -\mathbf{C}/w^{\alpha}$$

$$\text{as } N(1) << N_o, \text{ we have } \log(1-N(1)/N_o) \simeq -N(1)/N_o$$

$$\log(N(1)) \simeq \boldsymbol{\alpha}\log(w) + \log(N_o) - \log(\mathbf{C})$$

thus justifying our regression-based approach.

Computing the effect of α on sampling strategy efficiency

In order to compute the number of recovered clusters in breast cancer and cardiac tissue as a function of both r (number of regions) and w (width of FoV), we substituted equation (2) into equation (1):

$$N(r,w) = N_o * (1-\exp(-r*w^{\alpha}/C))$$

In order to compare both samples, we dropped the N_o term. We then selected three total area values (1.6 mm^2, 0.8 mm^2, and 0.32 mm^2) and computed N(r,w) for different ratios of r and w with a constant $r*w^2$ (total area) value.

Author Contributions

P.B. developed the methodology, implemented the R code, performed the IMC experiments and wrote the manuscript. D.S. participated to methodology development and implementation, S.E. performed IMC experiments, C.W. provided the samples and helped for methodology development and B.B. contributed to Funding Acquisition and manuscript writing.

Acknowledgements

We acknowledge the Bodenmiller lab members for critical reading and providing feedback on the manuscript. P.B. is funded by an EMBO postdoctoral fellowship (fellowship number ALT 427-2021).

References

Bendall, S.C., Simonds, E.F., Qiu, P., Amir, E.D., Krutzik, P.O., Finck, R., Bruggner, R.V., Melamed, R., Trejo, A., Ornatsky, O.I., et al. (2011). Single-cell mass cytometry of differential immune and drug responses across a human hematopoietic continuum. Science 332, 687–696.

Blondel, V.D., Guillaume, J.-L., Lambiotte, R., and Lefebvre, E. (2008). Fast unfolding of communities in large networks. Journal of Statistical Mechanics: Theory and Experiment 2008, P10008.

Eckel-Passow, J.E., Lohse, C.M., Sheinin, Y., Crispen, P.L., Krco, C.J., and Kwon, E.D. (2010). Tissue microarrays: one size does not fit all. Diagnostic Pathology 5, 48.

Giesen, C., Wang, H.A.O., Schapiro, D., Zivanovic, N., Jacobs, A., Hattendorf, B., Schüffler, P.J., Grolimund, D., Buhmann, J.M., Brandt, S., et al. (2014). Highly multiplexed imaging of tumor tissues with subcellular resolution by mass cytometry. Nature Methods 11, 417–422.

Greenwald, N.F., Miller, G., Moen, E., Kong, A., Kagel, A., Fullaway, C.C., McIntosh, B.J., Leow, K., Schwartz, M.S., Dougherty, T., et al. (2021). Whole-cell segmentation of tissue images with human-level performance using large-scale data annotation and deep learning. BioRxiv 2021.03.01.431313.

Harbeck, N., Penault-Llorca, F., Cortes, J., Gnant, M., Houssami, N., Poortmans, P., Ruddy, K., Tsang, J., and Cardoso, F. (2019). Breast cancer. Nat Rev Dis Primers 5, 1–31.

Jackson, H.W., Fischer, J.R., Zanotelli, V.R.T., Ali, H.R., Mechera, R., Soysal, S.D., Moch, H., Muenst, S., Varga, Z., Weber, W.P., et al. (2020). The single-cell pathology landscape of breast cancer. Nature 578, 615–620.

Jaitin, D.A., Kenigsberg, E., Keren-Shaul, H., Elefant, N., Paul, F., Zaretsky, I., Mildner, A., Cohen, N., Jung, S., Tanay, A., et al. (2014). Massively parallel single cell RNA-Seq for marker-free decomposition of tissues into cell types. Science 343, 776–779.

Lake, B.B., Chen, S., Sos, B.C., Fan, J., Kaeser, G.E., Yung, Y.C., Duong, T.E., Gao, D., Chun, J., Kharchenko, P.V., et al. (2018). Integrative single-cell analysis of transcriptional and epigenetic states in the human adult brain. Nat. Biotechnol. 36, 70–80.

Macosko, E.Z., Basu, A., Satija, R., Nemesh, J., Shekhar, K., Goldman, M., Tirosh, I., Bialas, A.R., Kamitaki, N., Martersteck, E.M., et al. (2015). Highly Parallel Genome-wide Expression Profiling of Individual Cells Using Nanoliter Droplets. Cell 161, 1202–1214.

Sebé-Pedrós, A., Saudemont, B., Chomsky, E., Plessier, F., Mailhé, M.-P., Renno, J., Loe-Mie, Y., Lifshitz, A., Mukamel, Z., Schmutz, S., et al. (2018). Cnidarian Cell Type Diversity and Regulation Revealed by Whole-Organism Single-Cell RNA-Seq. Cell 173, 1520-1534.e20.

Shah, S., Lubeck, E., Zhou, W., and Cai, L. (2016). In Situ Transcription Profiling of Single Cells Reveals Spatial Organization of Cells in the Mouse Hippocampus. Neuron 92, 342–357.

Titford, M. (2006). A Short History of Histopathology Technique. Journal of Histotechnology 29, 99–110.

Torre, E., Dueck, H., Shaffer, S., Gospocic, J., Gupte, R., Bonasio, R., Kim, J., Murray, J., and Raj, A. (2018). Rare Cell Detection by Single-Cell RNA Sequencing as Guided by Single-Molecule RNA FISH. Cell Syst 6, 171-179.e5.

Villani, A.-C., Satija, R., Reynolds, G., Sarkizova, S., Shekhar, K., Fletcher, J., Griesbeck, M., Butler, A., Zheng, S., Lazo, S., et al. (2017). Single-cell RNA-seq reveals new types of human blood dendritic cells, monocytes, and progenitors. Science 356, eaah4573.

Windhager, J., Bodenmiller, B., and Eling, N. (2021). An end-to-end workflow for multiplexed image processing and analysis (Bioinformatics).

(2008). Statistical analysis and modelling of spatial point patterns (Chichester, England ; Hoboken, NJ: John Wiley).

Figure 1: Use of spatial transcriptomic data to determine the optimal tissue sampling strategy for multiplexed imaging. (A) Analytical workflow used to simulate IMC of human tissues using spatial transcriptomic data. **(B)** Number of detected clusters vs. number of sampled regions for a bladder cancer dataset with 400 µm fields of view. Each point corresponds to the mean number of recovered clusters across 50 similar simulations, and vertical bars correspond to standard error. The red dashed line corresponds to the fitted function, and the two horizontal dashed lines correspond to the No parameter (red line) and the real total number of clusters (grey line). **(C)** Plot of τ for indicated samples from healthy and tumor samples. **(D)** Plot of τ values from healthy and tumor samples. The p-value was computed using a Kruskal-Wallis rank test. **(E)** Left panel: Mean number of clusters detected vs. number of sampled regions for FoV widths ranging from 200 to 600 µm for the cerebellum sample. Each point corresponds to the mean number of recovered cluster across 50 similar simulations, and vertical bars correspond to the standard error. Red dashed lines correspond to individual fits for each w value. Right panel: Relationship between τ and w for cerebellum sample. The dashed line corresponds to the linear regression after log10 transform. **(F)** Relationship between τ and w for the glioblastoma sample. The dashed line corresponds to the linear regression after log10 transform. **(G)** Left panel: Proportion of clusters recovered as a function of τ for the glioblastoma sample for indicated number of clusters. Each point corresponds to the mean number of recovered clusters across 50 similar simulations. For the sake of clarity, the error bars and fitted curves are not displayed. Right panel: Relationship between τ and the number of clusters for the glioblastoma sample. The dashed line corresponds to a linear regression. **(H)** Relationship between τ and the number of clusters for all studied samples. The dashed line corresponds to a linear regression.

Figure 2: Identification of a technology invariant measure of tissue complexity. (A) Experimental workflow to compare the results of spatial transcriptomic and IMC large-scale analysis. **(B)** Left panel: Number of recovered clusters vs. number of sampled regions for IMC lymph node data. Each point corresponds to the mean number of recovered clusters across 50 similar simulations, and vertical bars correspond to the standard error. The red dashed line corresponds to the fitted function. Middle panel: Number of detected clusters vs. number of sampled regions for FoVs ranging from 200 to 500 µm for the IMC (1) lymph node data. Each point corresponds to the mean number of recovered cluster across 50 similar simulations, and

vertical bars correspond to the standard error. The different red lines corresponds to individual fits for each w value. Right panel: Relationship τ and w for the IMC (1) lymph node data. The dashed line corresponds to the linear regression after log10 transform. **(C)** Left panel: Values of the τ for 400 µm width FoV for the lymph node datasets. Middle panel: Values of $\boldsymbol{\alpha}$ for the lymph node datasets. Right panel: Values of **C** for the lymph node datasets. **(D)** Comparison of $\boldsymbol{\alpha}$ values between the IMC breast cancer dataset and the five Visium breast cancer datasets. P-value was computed using a Kruskall-Wallis test. **(E)** Estimation of sampling strategy efficiency for breast cancer (left panel) and heart (right panel) samples. The dashed lines correspond to the possible values taken for a fixed area surface. **(F)** Proportions of detected clusters when area imaged (indicated by solid, dashed, or dotted lines) was fragmented for breast cancer (red lines) and heart (grey lines) datasets.

Supplementary Figure 1: (A) Distribution of R-squared values for the saturation model described in equation (1) across the different Visium datasets. **(B)** Distribution of R-squared values for the power-law model described in equation (2) across the different Visium datasets. **(C)** Approach used to estimate the impact of clustering granularity on τ value. **(D)** Relationship between τ and the number of clusters for the cerebellum sample.

Supplementary Figure 2: (A) Plot of $\boldsymbol{\alpha}$ values from healthy and tumor samples. The p-value was computed using a Kruskal-Wallis rank test. **(B)** Approach used to estimate $\boldsymbol{\alpha}$ from a set of small IMC FoVs.

Bost et al. Figure 1

A

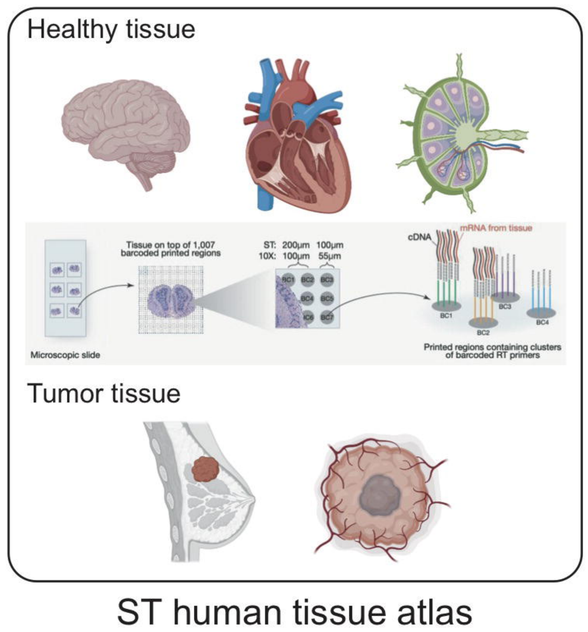

ST human tissue atlas

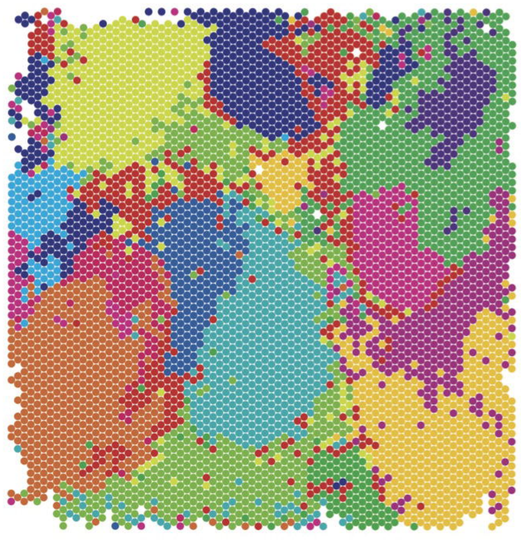

Data processing and analysis

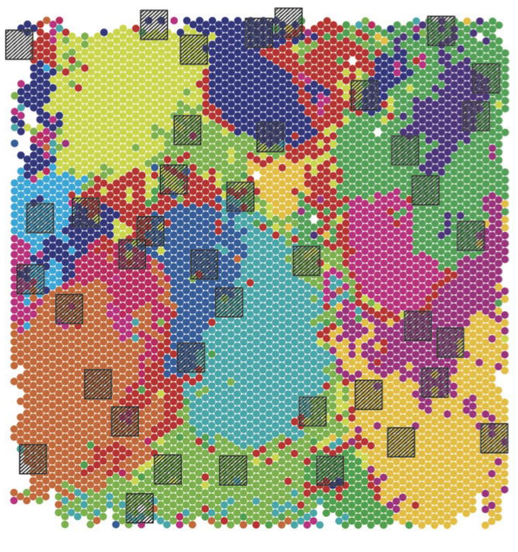

Simulation of spatial sampling

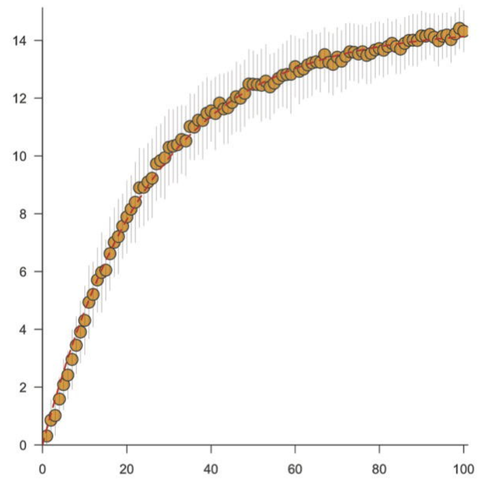

Estimation of tissue complexity

B

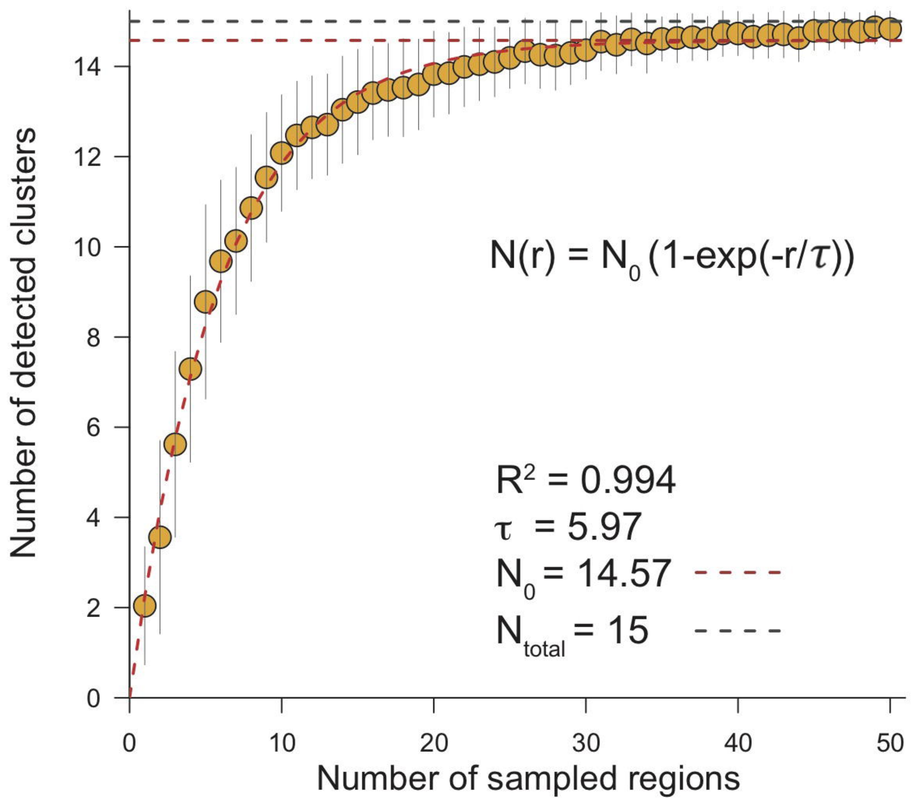

C

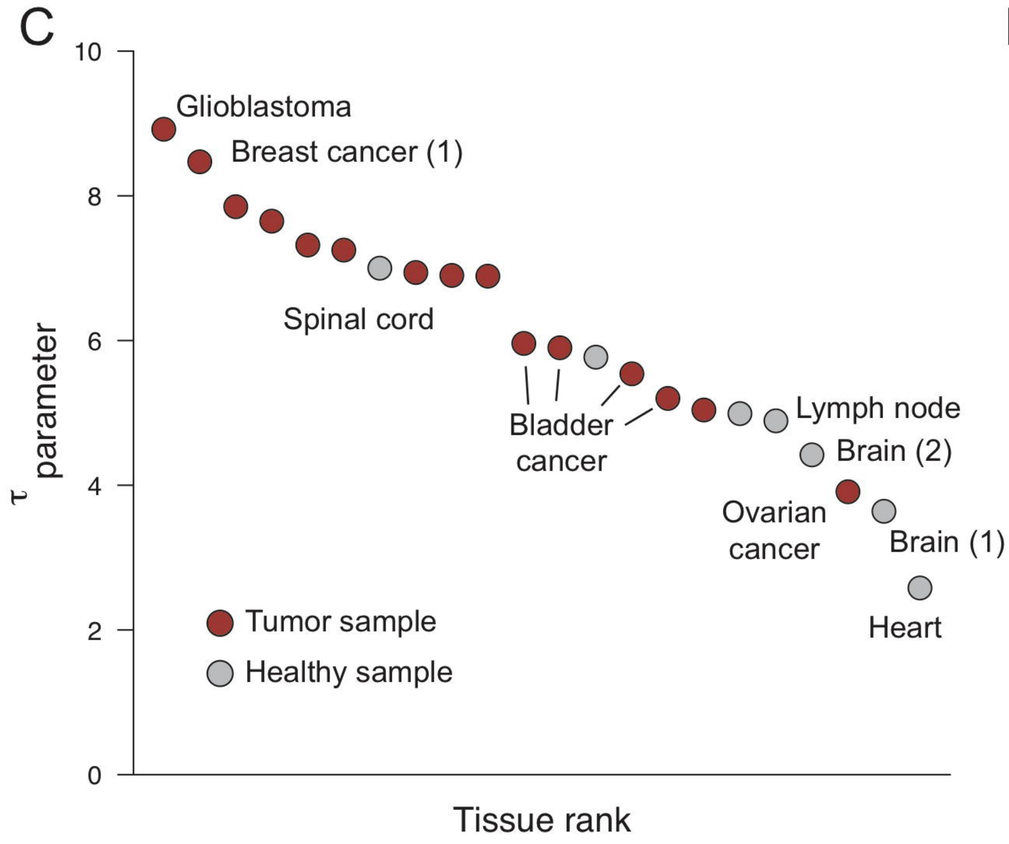

D

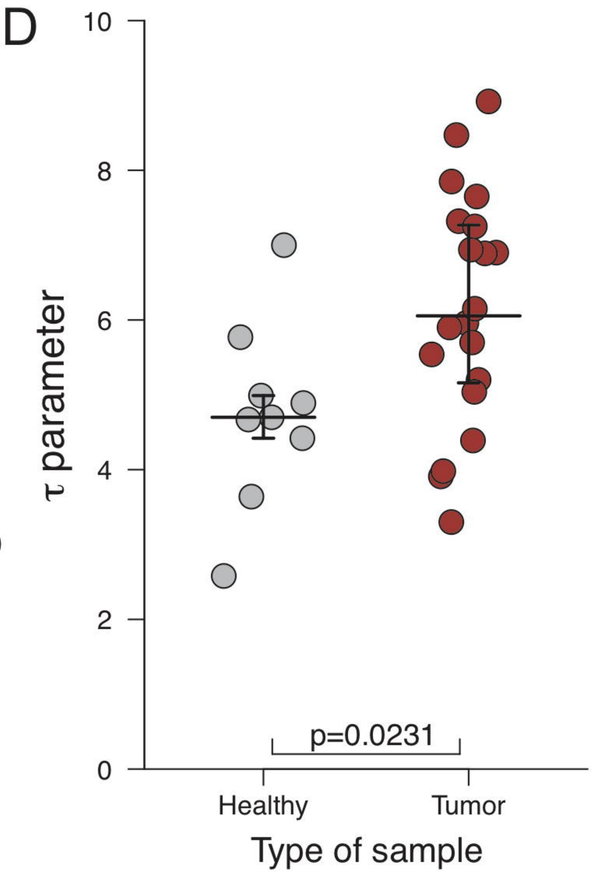

E

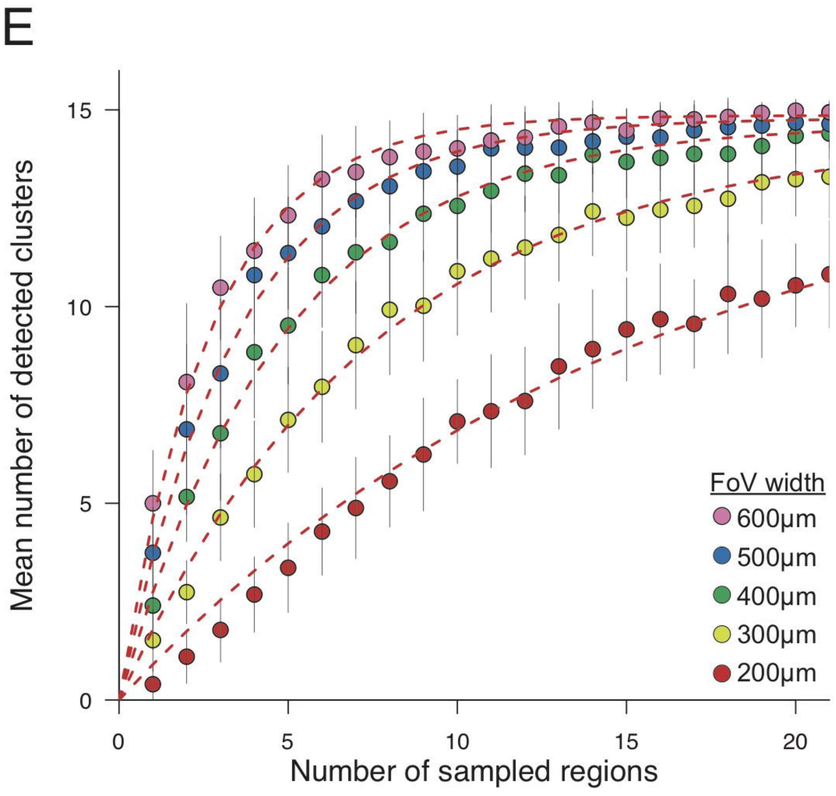

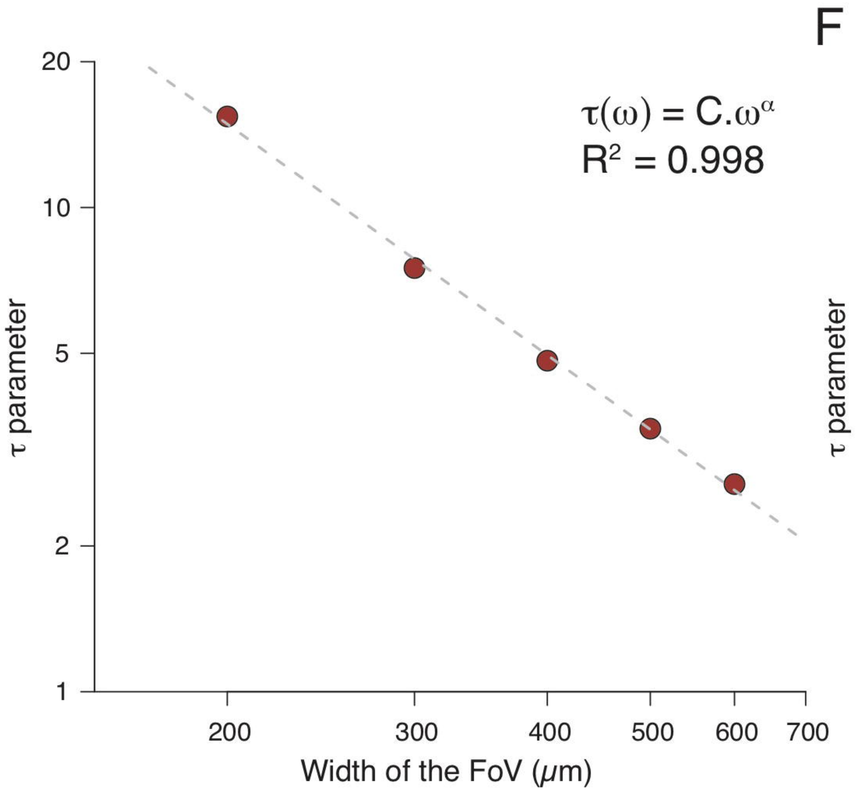

F

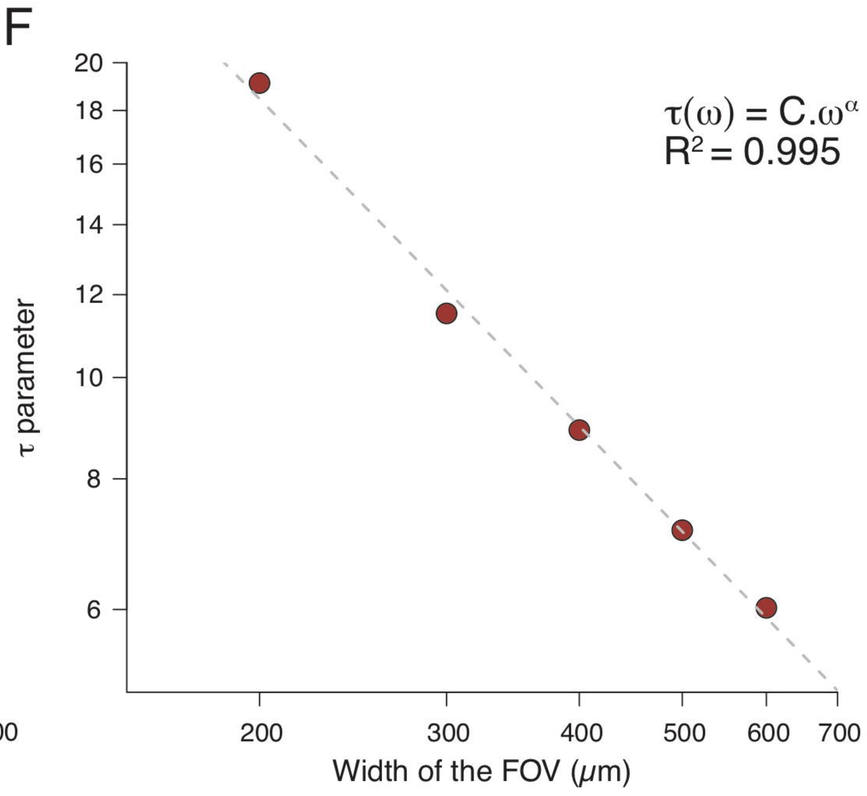

G

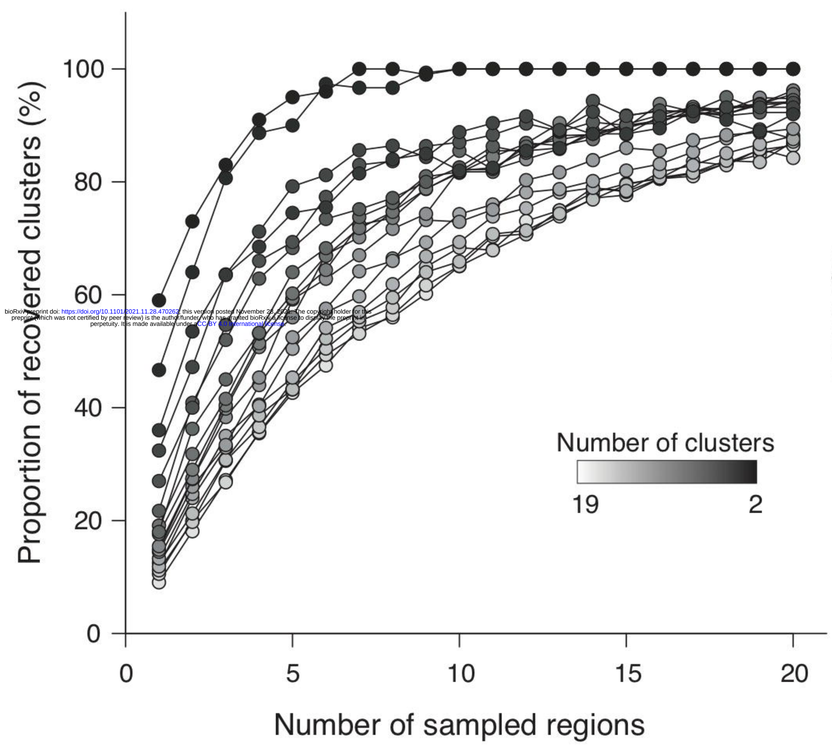

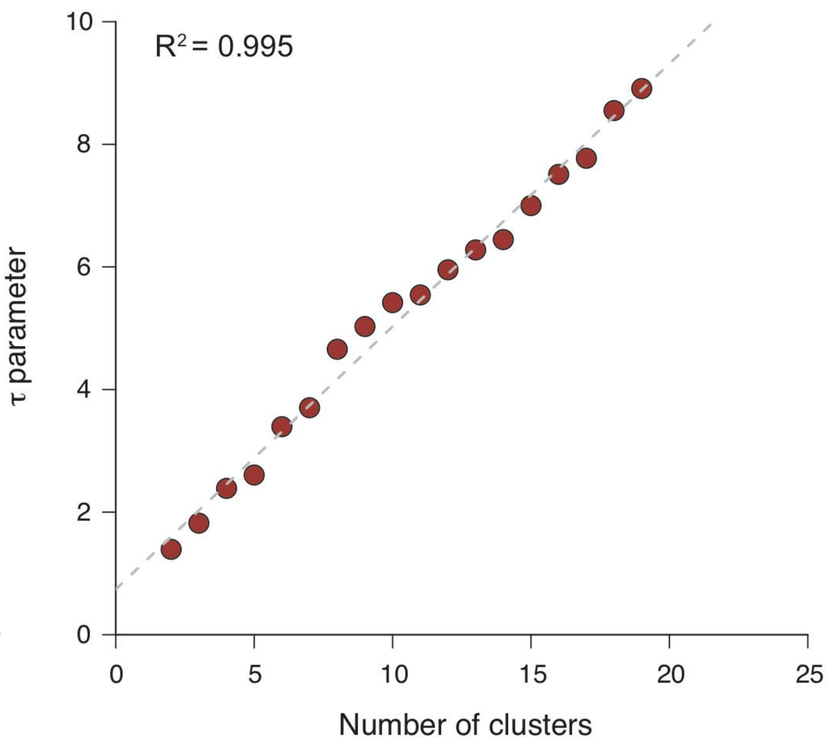

H

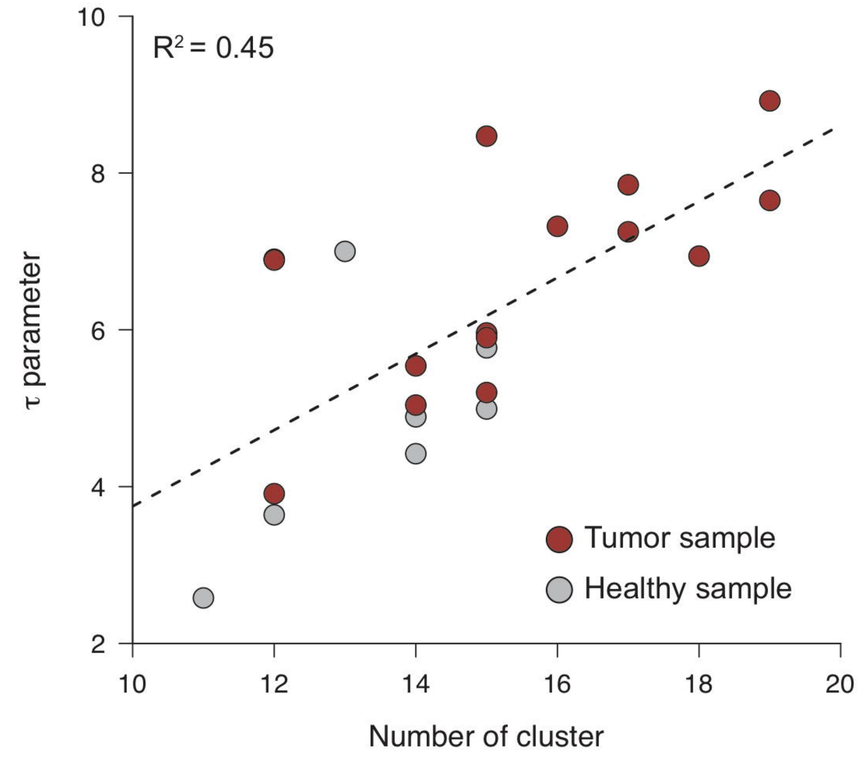

Bost et al. Figure 2

Bost et al. Supplementary Figure 1

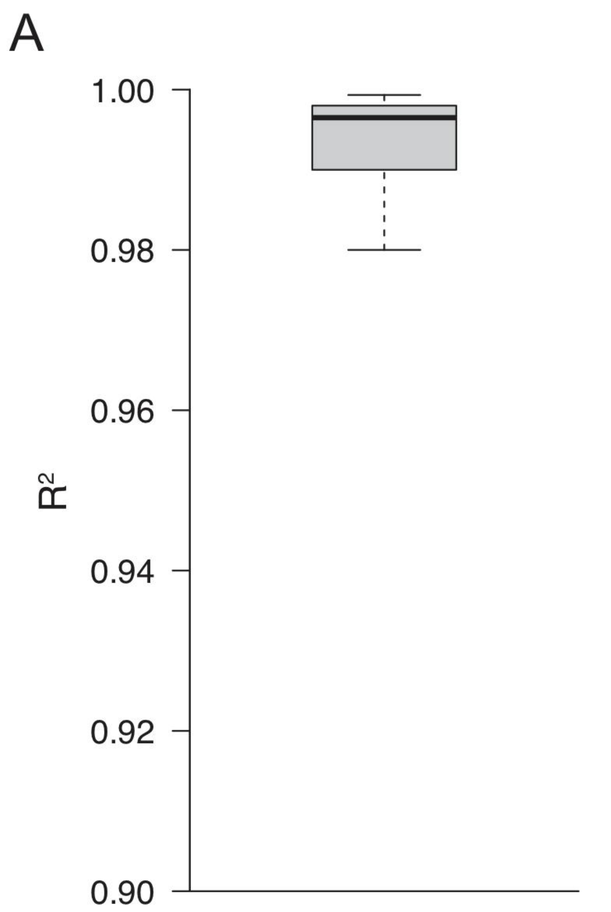

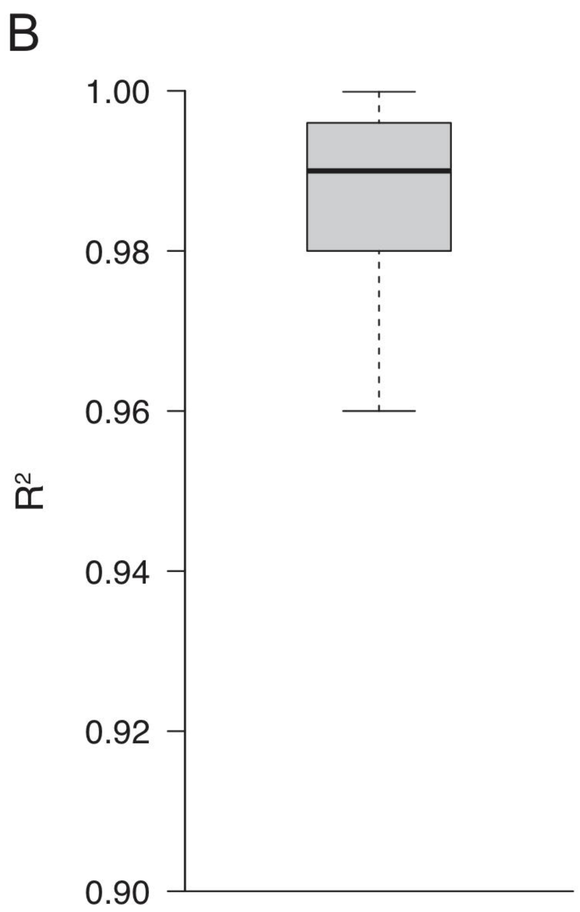

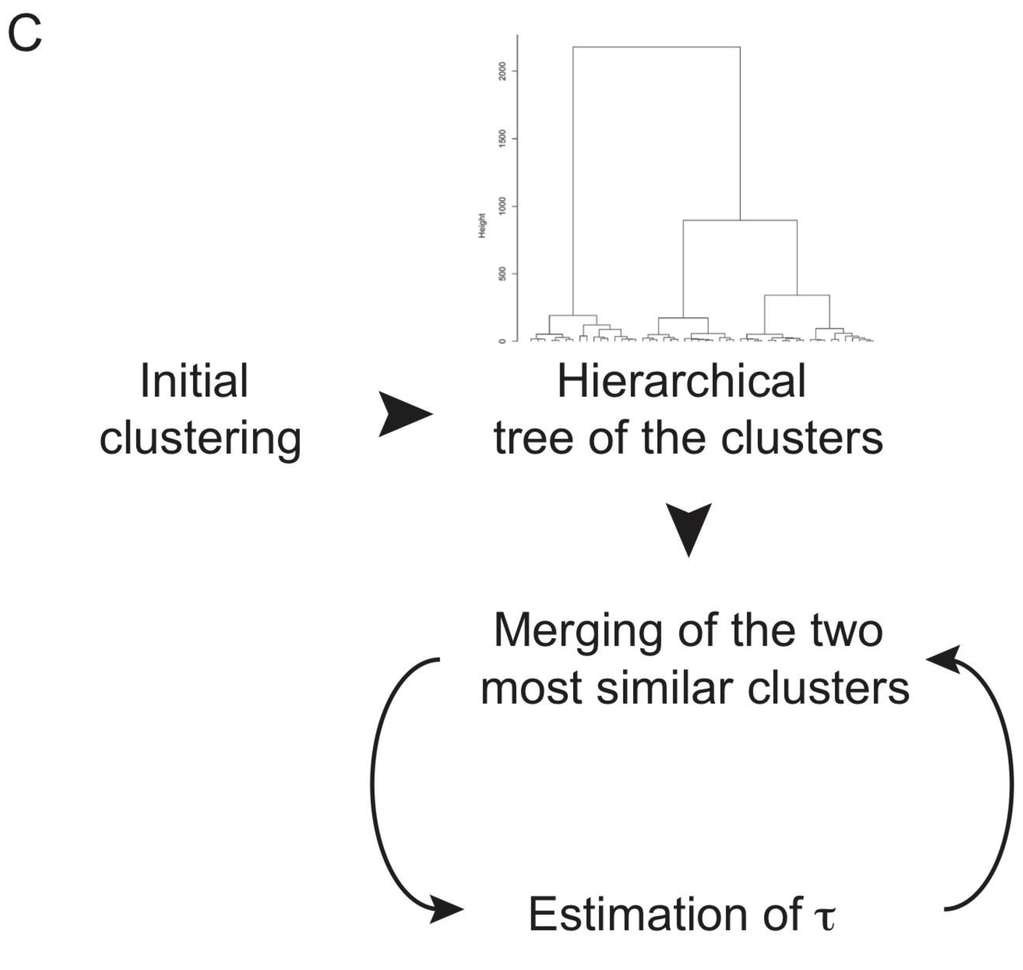

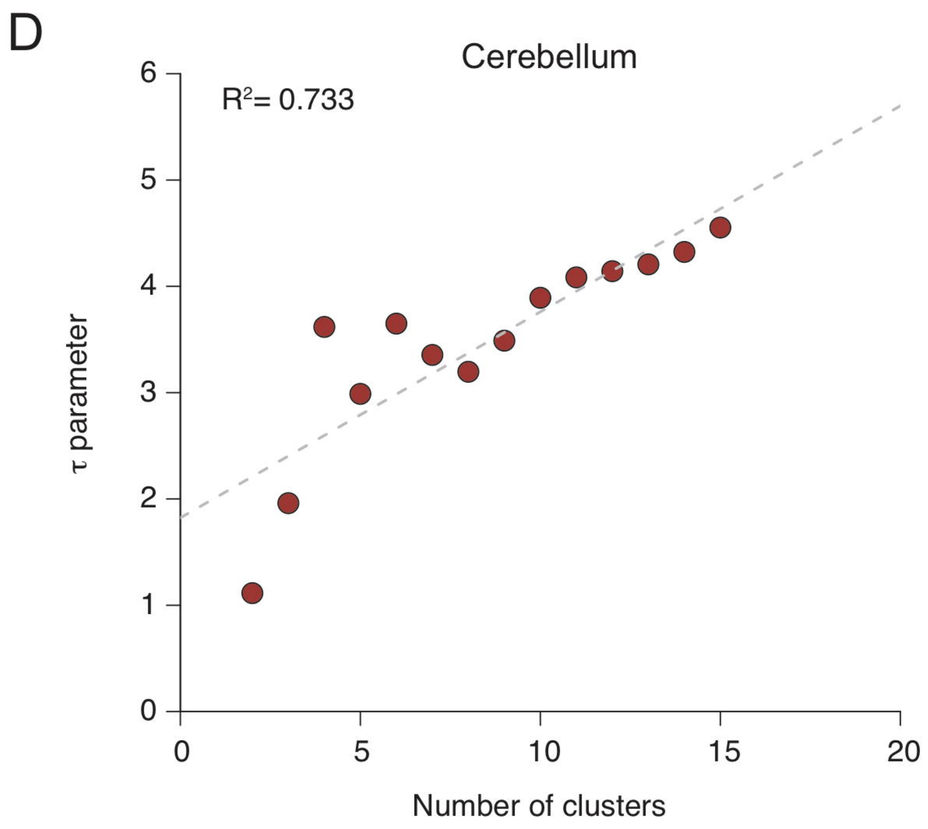

Bost et al. Supplementary Figure 2